

# Topological quantum walks in momentum space with a Bose-Einstein condensate

Dizhou Xie,<sup>1,\*</sup> Tian-Shu Deng,<sup>2,\*</sup> Teng Xiao,<sup>1</sup> Wei Gou,<sup>1</sup> Wei Yi,<sup>2,3,†</sup> and Bo Yan<sup>1,4,5,‡</sup>

<sup>1</sup>Zhejiang Province Key Laboratory of Quantum Technology and Device,  
Department of Physics and State Key Laboratory of Modern Optical Instrumentation,  
Zhejiang University, Hangzhou, Zhejiang, China, 310027

<sup>2</sup>CAS Key Laboratory of Quantum Information, University of Science and Technology of China, Hefei 230026, China

<sup>3</sup>CAS Center For Excellence in Quantum Information and Quantum Physics

<sup>4</sup>Collaborative Innovation Centre of Advanced Microstructures, Nanjing University, Nanjing, China, 210093

<sup>5</sup>Key Laboratory of Quantum Optics, Chinese Academy of Sciences, Shanghai 200800, China

(Dated: June 20, 2022)

We report the experimental implementation of discrete-time topological quantum walks of a Bose-Einstein condensate in momentum space. Introducing stroboscopic driving sequences to the generation of a momentum lattice, we show that the dynamics of atoms along the momentum lattice is dictated by a periodically driven Su-Schrieffer-Heeger model, which is equivalent to a discrete-time topological quantum walk. We directly measure the underlying topological invariants through time-averaged mean chiral displacements in different time frames, which are consistent with our experimental observation of topological phase transitions. The high tunability of the system further enables us to observe robust helical Floquet channels in the one-dimensional momentum lattice, which derive from the winding of Floquet quasienergy bands. Our experiment opens up the avenue of investigating discrete-time topological quantum walks using cold atoms, where the many-body environment and tunable interactions offer exciting new possibilities.

Exploring topological phases is a main theme in modern physics. Characterized by topological invariants which reflect the global geometric properties of the system wave function, topological phases host a range of fascinating features, which are robust to local perturbations and are potentially useful for applications in quantum information and quantum computation [1, 2]. Besides conventional topological materials in solid-state systems, topological phenomena also emerge away from equilibrium. For example, topological phases and emergent topological phenomena exist in non-Hermitian open systems [3–14], in periodically driven Floquet systems and quench processes [15–33], which have stimulated intense interest recently due to the rapid progress in synthetic quantum-simulation platforms such as cold atoms [34–37], photonics [38–52], phononics [53], and superconducting qubits [54].

A particularly interesting subject is topologies in periodically driven Floquet systems, which are shown to have a rich structure and host novel topological phases with no counterparts in static systems [20–23]. A paradigmatic example of topological Floquet dynamics is discrete-time quantum walks, which, besides potential applications in quantum information [55–57], have been widely used in photonics for the exploration of Floquet topological phases [38–47]. In cold atoms, whereas Floquet topological phases [34] and quantum walks [58] have been respectively implemented, quantum walks with topological properties are yet to be experimentally realized.

Here we report the experimental implementation of discrete-time topological quantum walks in momentum space for a Bose-Einstein condensate (BEC). Combining the generation of momentum lattice [59–63] with stroboscopic driving sequences, dynamics of the conden-

sate atoms is governed by a Su-Schrieffer-Heeger (SSH) Hamiltonian in momentum space with periodically driven parameters. It follows that dynamics of the system can be described as a discrete-time quantum walk which supports Floquet topological phases. Our experiment is in sharp contrast to previous studies of topological quantum walks in photonics [38–46], where dynamics are generated by Floquet operators rather than genuine Hamiltonians.

Since the topological classification of our Floquet system is  $Z \oplus Z$ , two distinct topological invariants exist [64]. We directly measure both topological invariants using time-averaged mean chiral displacement (A-MCD) by going to different time frames, and identify a topological phase transition as the driving parameters are tuned. The topological phase transition is then confirmed experimentally through second-statistical-moment measurements. We further demonstrate helical Floquet channels in the one-dimensional momentum lattice [65, 66], where atoms on different sublattice sites are locked into a leftward (rightward) unidirectional motion along the momentum lattice. These dispersionless channels originate from the winding of Floquet quasi-energy bands, and are protected by a pair of dynamic Chern numbers in parameter space. As a result, the unidirectional atom flow is robust against experimental errors.

*Discrete-time quantum walks in momentum space:-* As shown in Fig. 1, we implement discrete-time quantum walks in momentum space using Raman-induced momentum lattice with radio-frequency (RF) modulations. In previous experiments, momentum lattices have been realized for cold atoms, taking advantage of the precise control of momentum states with multi-frequency Raman beams [59–63]. In our experiment, we further introduce periodic switching of the odd- and even-frequency

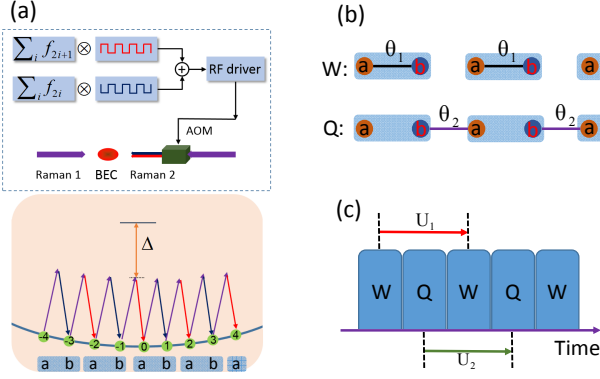


FIG. 1. (Color online) Experimental implementation of momentum-space discrete-time quantum walks with cold atoms. (a) Atoms in the BEC are coupled by counter-propagating Raman beams. One of the Raman beams (Raman 2) is imprinted with multiple-frequency components via an acoustic-optical modulator (AOM). The odd and even frequency components, marked by red and blue arrows, alternate in time, which are controlled by the radio-frequency (RF) driver. The periodically modulated Raman processes couple discretized momentum states, leading to a momentum lattice labeled by  $n \in \mathbb{Z}$  with nearest-neighbor Raman-assisted hopping. The staggered Raman couplings also enable us to define sublattice sites  $a$  and  $b$  along the momentum lattice. (b) Illustration of the effective time-evolution operators  $W$  and  $Q$ . Under  $W$ , the intra-cell couplings are turned on along the momentum lattice. Under  $Q$ , the inter-cell couplings are turned on. (c) Illustration of the two time frames, dictated by Floquet operators  $U_1$  and  $U_2$  (see definition in the main text), respectively.

components of the multi-frequency Raman lasers [see Fig. 1(a)]. This gives rise to a stroboscopic switching of the hopping terms between adjacent sites along the momentum lattice. Here the  $n$ -th site ( $n \in \mathbb{Z}$ ) along the lattice corresponds to the momentum  $p_n = n \times 2\hbar k$ , where  $k$  is the wave vector of the Raman lasers. As illustrated in Fig. 1(a), atoms on site  $n$  and  $n+1$  are coupled by a pair of Raman beams with an offset frequency  $f_n = (2n+1) \times 4E_r$ , where  $E_r$  is the recoil energy. In order to realize the switching of Raman couplings, the offset frequencies are divided into odd and even components depending on the parity of  $n$ . While these odd and even-frequency components are switched on and off by step functions through the RF driver, the effective Hamiltonian for the BEC atoms is given by

$$\hat{H} = \sum_m [w(t) |m, b\rangle \langle m, a| + q(t) |m+1, a\rangle \langle m, b| + H.c.], \quad (1)$$

where non-resonant Raman couplings are neglected. Here  $m$  labels the unit cell, and  $a$  and  $b$  label the sublattice sites within a unit cell. As shown in Fig. 1(a), adjacent momentum-lattice sites are mapped to sublattice sites  $a$  and  $b$  of a unit cell in Eq. (1), such that

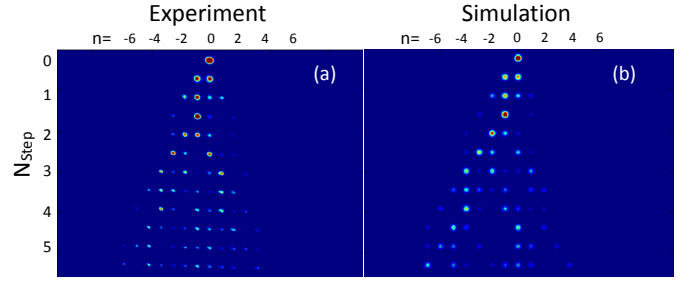


FIG. 2. (Color online) Experimental demonstration of a typical discrete-time quantum-walk dynamics in momentum space. For the experiment, we have  $(\theta_1, \theta_2) = (\pi/4, \pi/4)$ .

$|m, a\rangle$  ( $|m, b\rangle$ ) corresponds to the momentum-lattice site  $n = 2m$  ( $n = 2m+1$ ). Importantly, the step-wise Raman-induced hopping rates  $w(t)$  and  $q(t)$  satisfy  $w(t) + q(t) = -\frac{\Omega}{2}$ , where  $\Omega$  is the Raman-coupling rate and  $w(t)$  is given by

$$w(t) = \begin{cases} -\frac{\Omega}{2}, & jT < t \leq jT + t_w \\ 0, & jT + t_w < t \leq (j+1)T \end{cases}. \quad (2)$$

Here  $j \in \{0, 1, 2, \dots\}$ ,  $T = t_w + t_q$ , and  $t_w$  and  $t_q$  are pulse durations for Raman processes with even- and odd-frequency components, respectively. The effective Hamiltonian Eq. (1) captures the dynamics well as long as  $\Omega \ll 4E_r$  [67], which is the case in our experiment.

Dynamics under the periodically driven SSH model in Eq. (1) can be further mapped to discrete-time quantum-walk dynamics governed by Floquet operators. As illustrated in Fig. 1(b), when the even-frequency Raman coupling is turned on, intra-cell hopping  $w(t)$  in Eq. (1) is finite while  $q(t) = 0$ . It follows that the corresponding time-evolution operator  $W(\theta_1)$  is given by

$$W(\theta_1) |m, a(b)\rangle = \cos \theta_1 |m, a(b)\rangle + i \sin \theta_1 |m, b(a)\rangle, \quad (3)$$

where  $\theta_1 = \Omega t_w/2$ . Similarly, when the odd-frequency Raman coupling is turned on, inter-cell hopping  $q(t)$  is finite and  $w(t) = 0$ . It follows that the time-evolution operator  $Q(\theta_2)$  is

$$Q(\theta_2) |m, a(b)\rangle = \cos \theta_2 |m, a(b)\rangle + i \sin \theta_2 |m \mp 1, b(a)\rangle, \quad (4)$$

where  $\theta_2 = \Omega t_q/2$ . Note that the condition  $t_w + t_q = T$  translates to  $\theta_1 + \theta_2 = \Omega T/2$ . The overall dynamics of the system is thus governed the Floquet operator  $U = Q(\theta_2)W(\theta_1)$ , driving a discrete-time quantum-walk dynamics.

Experimentally, we prepare a BEC with  $\sim 6 \times 10^4$  atoms in a crossed dipole trap with trapping frequencies  $2\pi \times (115, 40, 100)$  Hz. We generate the momentum lattice

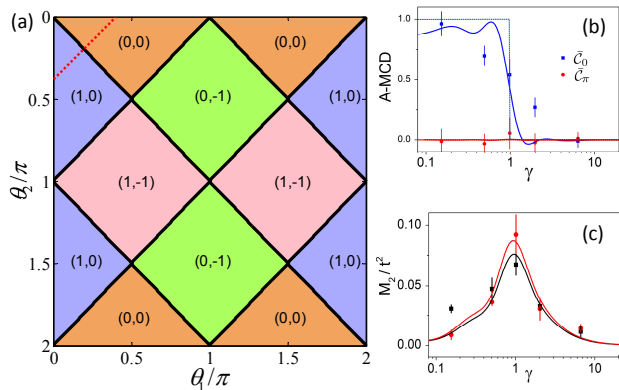


FIG. 3. (Color online) (a) Topological phase diagram of our discrete-time quantum walk. Topological invariants  $(C_0, C_\pi)$  are shown on the plane of  $(\theta_1, \theta_2)$ . The dashed red line indicates the parameters traversed in (b)(c). (b) Experimentally measured A-MCD for a six-step quantum walk. The dashed blue (red) line shows the variation of  $C_0$  ( $C_\pi$ ). (c) Experimentally measured second statistical moment  $M_2/t^2$  for dynamics governed by  $U_1$  (black) and  $U_2$  (red), respectively. In (b)(c), the experimental data (dots with error bars) agree well with results from numerical simulations (solid lines), which reveal a topological phase transition near  $\gamma = 1$ .

following the procedure outlined in Ref. [63]. Quantum-walk dynamics are introduced by periodical modulation of the Raman pulses inducing the momentum lattice. For detection, we turn off all the dipole trap and Raman beams, and take an absorption image after 20ms time of flight, from which atom populations in different momentum states are extracted. For all our experiments, we set  $\Omega = 2\pi \times 2.3\text{kHz}$  and  $E_r \approx 2.03\text{kHz}$ , while  $\theta_1$  and  $\theta_2$  are tuned by adjusting pulse durations  $t_w$  and  $t_q$ . A typical experimental measurement for a homogeneous discrete-time quantum-walk dynamics is shown in Fig. 2, where a ballistic spreading of population, typical for discrete-time quantum walks, is observed. Here we fix  $T \approx 0.22\text{ms}$  and  $t_w = t_q$ .

*Detecting topological properties:*- Quantum walks governed by the Floquet operator  $U = Q(\theta_2)W(\theta_1)$  support Floquet topological phases, which are characterized by a pair of winding numbers defined in distinct time frames. As illustrated in Fig. 1(c), these time frames are associated with the Floquet operators

$$\begin{aligned} U_1 &= W\left(\frac{\theta_1}{2}\right)Q(\theta_2)W\left(\frac{\theta_1}{2}\right), \\ U_2 &= Q\left(\frac{\theta_2}{2}\right)W(\theta_1)Q\left(\frac{\theta_2}{2}\right), \end{aligned} \quad (5)$$

which have chiral symmetry  $\Gamma U_\alpha \Gamma^{-1} = U_\alpha^{-1}$  ( $\alpha = 1, 2$ ) with  $\Gamma = \sigma_z$ , and give rise to winding numbers  $C_1$  and  $C_2$ , respectively. Following the practice in Ref. [64], we define topological invariants  $(C_0, C_\pi) = (\frac{C_1 + C_2}{2}, \frac{C_1 - C_2}{2})$ , which dictate the number of topological edge states with quasienergies  $E = 0$  and  $E = \pi$ , respectively, through the

bulk-boundary correspondence. The topological phase diagram of the system is shown in Fig. 3(a), where topological invariants  $(C_0, C_\pi)$  are plotted as functions of the Raman-coupling parameters  $(\theta_1, \theta_2)$ .

To experimentally demonstrate topological features of the momentum-space quantum walk, we experimentally probe the topological invariants  $(C_0, C_\pi)$ , and confirm topological phase transitions by monitoring dynamics of condensate atoms in momentum space. Quantum walks in different time frames are implemented by applying different sequence of Raman pulses which correspond to  $U_1$  and  $U_2$ , respectively. Here we fix  $T \approx 0.16\text{ms}$  and adjust  $t_w$  and  $t_q$ , which corresponds to  $\theta_1 + \theta_2 = 3\pi/8$ , as shown by the red dashed line in Fig. 3(a).

First, we directly probe topological invariants  $(C_0, C_\pi)$  by detecting mean chiral displacements [40]. We initialize atoms in the  $n = 0$  state, let them evolve on the momentum lattice, and take time-of-flight images at different time steps. To suppress experimental errors induced by imperfect control of pulse durations in  $W$  and  $Q$  [67], we measure the A-MCD for an  $N$ -step quantum walk, defined as

$$\bar{C}_\alpha = \frac{2}{N} \sum_{N_{\text{step}}=1}^N \sum_m m \left[ P_{m,a}^{(\alpha)}(N_{\text{step}}) - P_{m,b}^{(\alpha)}(N_{\text{step}}) \right], \quad (6)$$

where  $\alpha \in \{1, 2\}$  indicates the time frame, and  $P_{m,a(b)}^{(\alpha)}(N_{\text{step}})$  is the measured atom population in the state  $|m, a(b)\rangle$  at the  $N_{\text{step}}$ -th step ( $N_{\text{step}} \in \mathcal{N}$ ) for the dynamics under  $U_\alpha$ . Performing the measurements in both time frames, we construct  $\bar{C}_{0,\pi} = \frac{1}{2}(\bar{C}_1 \pm \bar{C}_2)$ , which should approach  $C_{0,\pi}$  in the long-time limit. In our experiment, as shown in Fig. 3(b), the measured A-MCDs agree well with theoretical predictions after a six-step quantum walk.

An important observation of the measured A-MCD is the occurrence of a topological phase transition near  $\gamma = 1$  ( $\gamma = \theta_1/\theta_2$ ), where the numerically calculated winding numbers  $C_1$  and  $C_2$  undergo abrupt changes. To confirm this, we measure the second-statistical moment  $M_2^{(\alpha)}$ , which is defined as

$$M_2^{(\alpha)} = \sum_m m^2 \left[ P_{m,a}^{(\alpha)}(N_{\text{step}}) + P_{m,b}^{(\alpha)}(N_{\text{step}}) \right] \quad (7)$$

for the  $N_{\text{step}}$ -th step. In the long-time limit,  $M_2^{(\alpha)}$  should peak at the topological phase boundary under  $U_\alpha$  [39], where the corresponding winding number undergoes an abrupt jump. In Fig. 3(c), we show measured  $M_2^{(\alpha)}$  after six time steps. The measured peaks in  $M_2^{(\alpha)}$  for both time frames are located near  $\gamma = 1$ , consistent with theoretical predictions. We note that the measured topological invariants and phase transitions are also consistent with edge-state measurement when an open boundary is imposed [67].

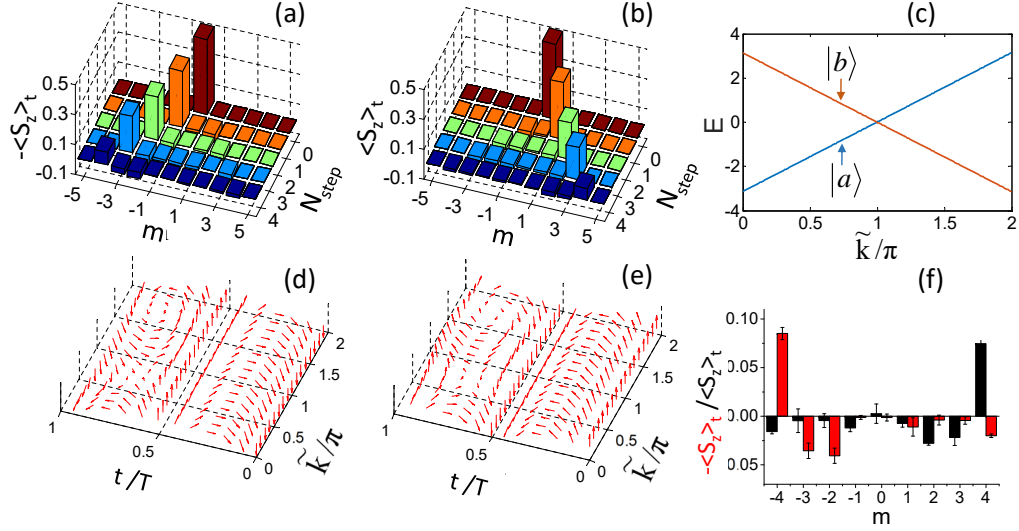


FIG. 4. (Color online) Observation of helical Floquet channels with  $(\theta_1, \theta_2) = (\pi/2, \pi/2)$ . (a) Measured  $-\langle S_z \rangle_t$  shows a unidirectional leftward flow for atoms initialized in  $|0, b\rangle$ . (b) Measured  $\langle S_z \rangle_t$  shows a unidirectional rightward flow for atoms initialized in  $|0, a\rangle$ . (c) Quasienergy dispersion for  $(\theta_1, \theta_2) = (\pi/2, \pi/2)$ . (d)(e) Space-time spin textures corresponding to dynamics in (a)(b), respectively. (f) Measured  $\pm\langle S_z \rangle_t$  for  $N_{\text{step}} = 4$ . Red (black) bars correspond to  $-\langle S_z \rangle_t$  ( $\langle S_z \rangle_t$ ) for atoms initialized in  $|0, b\rangle$  ( $|0, a\rangle$ ).

*Robust helical Floquet channels:*— The high tunability of our configuration further enables us to observe robust helical Floquet channels in the one-dimensional momentum lattice [65, 66]. These helical Floquet channels derive from windings of the Floquet quasienergy bands, and manifest themselves as unidirectional flow of atoms along the momentum lattice. To observe the phenomenon, we evolve the system under the Floquet operator  $U_h = Q(\pi/2)W(\pi/2)$ , which corresponds to fixing  $T \approx 0.44\text{ms}$  and  $t_w = t_q$ . We then measure  $\langle S_z \rangle_t$  as a function of  $m$  at each time step, where  $S_z = (|m, a\rangle\langle m, a| - |m, b\rangle\langle m, b|)/2$ . More generally, we define the pseudo-spin operators  $S_\beta$  ( $\beta = x, y, z$ ) with  $S_\beta = \frac{1}{2}|m, \mu\rangle\sigma_\beta^{\mu\nu}\langle m, \nu|$ , where  $\mu, \nu \in \{a, b\}$  and  $\sigma_\beta^{\mu\nu}$  is the corresponding Pauli matrix element. In a perfect helical Floquet channel, pseudo-spins with spin-down (spin-up) polarization along the  $z$  axis should propagate to the left (right), demonstrating a “spin-momentum locking” behavior discussed in Ref. [65]. Such a behavior is clearly observed in Fig. 4(a)(b), where atoms initialized in  $|m = 0, b\rangle$  ( $|m = 0, a\rangle$ ) propagate to the left (right) along the momentum lattice during the quantum-walk dynamics.

Such a behavior originates from the winding of the Floquet quasienergy bands. In Fig. 4(c), we show the quasienergy of  $U_h$ . Whereas the quasienergy spectrum is gapless, thus invalidating the calculation of winding numbers defined on the one-dimensional Brillouin zone of the momentum lattice, the spectrum clearly shows the winding of Floquet quasienergy bands [15]. Importantly, the decoupled linear dispersions of atoms in states  $|a\rangle$  and  $|b\rangle$

underlie the dispersionless helical Floquet channels observed in Fig. 4(a)(b). Formally, the Fourier components of  $U_h$  can be decomposed into  $U_{\tilde{k}}^{(\mu)}$  ( $\mu = a, b$ ), which are Floquet operators associated with the two sublattice sites. Here  $\tilde{k}$  belongs to the first Brillouin zone (1BZ) of the effective Hamiltonian Eq. (1). The Floquet winding numbers are then defined as [15, 65]

$$\nu^{(\mu)} = \frac{1}{2\pi i} \int_{\text{1BZ}} d\tilde{k} \text{Tr}[U_{\tilde{k}}^{(\mu)} \partial_{\tilde{k}} U_{\tilde{k}}^{(\mu)\dagger}], \quad (8)$$

with  $\nu^{(a)} = 1$  and  $\nu^{(b)} = -1$  under  $U_h$ . These Floquet winding numbers are equivalent to dynamic Chern numbers defined on the  $\tilde{k}$ - $t$  manifold, which can be visualized as dynamic-skyrmion structures in the pseudo-spin micromotion of the atoms [see Figs. 4(d)(e)]. Here the pseudo-spin textures are given by  $\mathbf{n}(\tilde{k}, t) = \sum_{\beta=x,y,z} \langle S_\beta \rangle_t \mathbf{e}_\beta$  in each  $\tilde{k}$  sector ( $\mathbf{e}_\beta$  being the unit vector of the corresponding direction), with atoms initialized in  $|b\rangle$  and  $|a\rangle$ , respectively, for Figs. 4(d) and (e).

Due to their topological origin, a remarkable feature of the helical Floquet channels is their robustness against perturbations, which manifests in the robustness of the spin-momentum locking. In our experiment, the fact that we observe these channels at all relies upon this very robustness. Specifically, due to experimental decoherence and fluctuations in the pulse durations, atoms in different helical Floquet channel are inevitably coupled to each other. In Fig. 4(f), we plot the distribution of  $\langle S_z \rangle_t$  along the momentum lattice at  $N_{\text{step}} = 4$ . Whereas the peak values decay below 0.1, indicating atom loss from the corresponding helical Floquet channel, the highest peak is

still on the left- (right-) most unit cell for atoms initialized in  $|b\rangle$  ( $|a\rangle$ ), such that the unidirectional flows are still observable. Further, atoms coupled out of a given Floquet channel lag behind the highest peak in propagation and reverse their pseudo-spin polarizations, suggesting the robustness of spin-momentum locking.

*Conclusion:-* We experimentally implement a stroboscopic driving of ultracold atoms on a momentum lattice, thus realizing discrete-time quantum-walk dynamics using cold atoms. We investigate in detail topological properties of the quantum-walk dynamics, including measuring topological invariants, probing topological phase transitions, and observing robust helical Floquet channels. By realizing discrete-time quantum-walk dynamics in a quantum many-body system via stroboscopic driving of the Hamiltonian, our experiment differs fundamentally from existing studies of photonic quantum-walk dynamics where the dynamics is driven by the propagation of classical light or photons rather than by Hamiltonians. Based on the flexible controls available in cold atoms, it would be interesting to explore topological quantum-walk dynamics under interaction, in the presence of non-Hermiticity, or in higher dimensions.

We acknowledge the support from the National Key R&D Program of China under Grant No.2018YFA0307200, National Natural Science Foundation of China under Grant No. 91636104, Natural Science Foundation of Zhejiang province under Grant No. LZ18A040001, and the Fundamental Research Funds for the Central Universities. W. Y. acknowledges support from the National Key Research and Development Program of China (Grant Nos. 2016YFA0301700 and 2017YFA0304100). D. X. and T.-S. D. contributed equally to this work.

---

\* These authors contributed equally to this work

† wyiz@ustc.edu.cn

‡ yanbohang@zju.edu.cn

- [1] M. Z. Hasan and C. L. Kane, *Rev. Mod. Phys.* **82**, 3045 (2010).
- [2] X.-L. Qi and S.-C. Zhang, *Rev. Mod. Phys.* **83**, 1057 (2011).
- [3] M. S. Rudner and L. S. Levitov, *Phys. Rev. Lett.* **102**, 065703 (2009).
- [4] K. Esaki, M. Sato, K. Hasebe, and M. Kohmoto, *Phys. Rev. B* **84**, 205128 (2011).
- [5] S.-D. Liang and G.-Y. Huang, *Phys. Rev. A* **87**, 012118 (2013).
- [6] B. Zhu, R. Lü, and S. Chen, *Phys. Rev. A* **89**, 062102 (2014)
- [7] T. E. Lee, *Phys. Rev. Lett.* **116**, 133903 (2016).
- [8] S. Yao and Z. Wang, *Phys. Rev. Lett.* **121**, 086803 (2018).
- [9] S. Yao, F. Song, and Z. Wang, *Phys. Rev. Lett.* **121**, 136802 (2018).
- [10] F. K. Kunst, E. Edvardsson, J. C. Budich, and E. J. Bergholtz, *Phys. Rev. Lett.* **121**, 026808 (2018).
- [11] Z. Gong, Y. Ashida, K. Kawabata, K. Takasan, S. Higashikawa, and M. Ueda, *Phys. Rev. X* **8**, 031079 (2018).
- [12] K. Kawabata, K. Shiozaki, M. Ueda, and M. Sato, arXiv:1812.09133.
- [13] H. Zhou and J. Y. Lee *Phys. Rev. B* **99**, 235112 (2019).
- [14] A. Ghatak and T. Das, *J. Phys.: Condens. Matter* **31**, 263001 (2019).
- [15] T. Kitagawa, E. Berg, M. Rudner, and E. Demler, *Phys. Rev. B* **82**, 235114 (2010).
- [16] L. Jiang, T. Kitagawa, J. Alicea, A. R. Akhmerov, D. Pekker, G. Refael, J. I. Cirac, E. Demler, M. D. Lukin, and P. Zoller, *Phys. Rev. Lett.* **106**, 220402 (2011).
- [17] J. Eisert, M. Friesdorf, and C. Gogolin, *Nat. Phys.* **11**, 124 (2015).
- [18] M. D. Caio, N. R. Cooper, and M. J. Bhaseen, *Phys. Rev. Lett.* **115**, 236403 (2015).
- [19] L. D'Alessio and M. Rigol, *Nat. Commun.* **6**, 8336 (2015).
- [20] M. S. Rudner, N. H. Lindner, E. Berg, and M. Levin, *Phys. Rev. X* **3**, 031005 (2013).
- [21] N. Goldman and J. Dalibard, *Phys. Rev. X* **4**, 031027 (2016).
- [22] A. C. Potter, T. Morimoto, and A. Vishwanath, *Phys. Rev. X* **6**, 041001 (2016).
- [23] V. Khemani, A. Lazarides, R. Moessner, and S. L. Sondhi, *Phys. Rev. Lett.* **116**, 250401 (2016).
- [24] M. Heyl, A. Polkovnikov, and S. Kehrein, *Phys. Rev. Lett.* **110**, 135704 (2013).
- [25] J. C. Budich and M. Heyl, *Phys. Rev. B* **93**, 085416 (2016).
- [26] Z. Huang and A. V. Balatsky, *Phys. Rev. Lett.* **117**, 086802 (2016).
- [27] Y. Hu, P. Zoller, and J. C. Budich, *Phys. Rev. Lett.* **117**, 126803 (2016).
- [28] J. H. Wilson, J. C. W. Song, and G. Refael, *Phys. Rev. Lett.* **117**, 235302 (2016).
- [29] C. Wang, P. Zhang, X. Chen, J. Yu, and H. Zhai, *Phys. Rev. Lett.* **118**, 185701 (2017).
- [30] C. Yang, L. Li, and S. Chen, *Phys. Rev. B* **97**, 060304(R) (2018).
- [31] Z. Gong and M. Ueda, *Phys. Rev. Lett.* **121**, 250601 (2018).
- [32] L. Zhang, L. Zhang, S. Niu, X. -J. Liu, *Sci. Bull.* **63**, 1385 (2018).
- [33] X. Qiu, T.-S. Deng, Y. Hu, P. Xue, and W. Yi, arXiv:1806.10268.
- [34] G. Jotzu, M. Messer, R. Desbuquois, M. Lebrat, T. Uehlinger, D. Greif, and T. Esslinger, *Nature* **515**, 237 (2014).
- [35] N. Fläschner, B. S. Rem, M. Tarnowski, D. Vogel, D.-S. Lühmann, K. Sengstock, and C. Weitenberg, *Science* **352**, 1091 (2016).
- [36] N. Fläschner, D. Vogel, M. Tarnowski, B. S. Rem, D.-S. Lühmann, M. Heyl, J. C. Budich, L. Mathey, K. Sengstock, and C. Weitenberg, *Nat. Phys.* **14**, 265 (2018).
- [37] W. Sun, C.-R. Yi, B.-Z. Wang, W.-W. Zhang, B. C. Sanders, X.-T. Xu, Z.-Y. Wang, J. Schmiedmayer, Y. Deng, X.-J. Liu, S. Chen, and J.-W. Pan, *Phys. Rev. Lett.* **121**, 250403 (2018).
- [38] T. Kitagawa, M. A. Broome, A. Fedrizzi, M. S. Rudner, E. Berg, I. Kassal, A. Aspuru-Guzik, E. Demler, and A. G. White, *Nat. Commun.* **3**, 882 (2012).
- [39] F. Cardano, M. Maffei, F. Massa, B. Piccirillo, C. de Lisi, G. De Filippis, V. Cataudella, E. Santamato, and

- L. Marrucci, *Nat. Commun.* **7**, 11439 (2016).
- [40] F. Cardano, A. D'Errico, A. Dauphin, M. Maffei, B. Piccirillo, C. de Lisio, G. De Filippis, V. Cataudella, E. Santamato, L. Marrucci, M. Lewenstein, and P. Massignan, *Nat. Commun.* **8**, 15516 (2017).
- [41] S. Barkhofen, T. Nitsche, F. Elster, L. Lorz, A. Gbris, I. Jex, and C. Silberhorn *Phys. Rev. A* **96**, 033846 (2017).
- [42] L. Xiao, X. Zhan, Z. H. Bian, K. K. Wang, X. Zhang, X. P. Wang, J. Li, K. Mochizuki, D. Kim, N. Kawakami, W. Yi, H. Obuse, B. C. Sanders, and P. Xue, *Nat. Phys.* **13**, 1117 (2017).
- [43] X. Zhan, L. Xiao, Z. Bian, K. Wang, X. Qiu, B. C. Sanders, W. Yi, and P. Xue, *Phys. Rev. Lett.* **119**, 130501 (2017).
- [44] X.-Y. Xu, Q.-Q. Wang, W.-W. Pan, K. Sun, J.-S. Xu, G. Chen, J.-S. Tang, M. Gong, Y.-J. Han, C.-F. Li, and G.-C. Guo, *Phys. Rev. Lett.* **120**, 260501 (2018).
- [45] B. Wang, T. Chen and X. Zhang, *Phys. Rev. Lett.* **121**, 100501 (2018).
- [46] C. Chen, X. Ding, J. Qin, Y. He, Y.-H. Luo, M.-C. Chen, C. Liu, X.-L. Wang, W.-J. Zhang, H. Li, L.-X. You, Z. Wang, D.-W. Wang, B. C. Sanders, C.-Y. Lu and J.-W. Pan, *Phys. Rev. Lett.* **121**, 100502 (2018).
- [47] A. D'Errico, F. Cardano, M. Maffei, A. Dauphin, R. Barboza, C. Esposito, B. Piccirillo, M. Lewenstein, P. Massignan, L. Marrucci, arXiv:1811.04001
- [48] S. Weimann, M. Kremer, Y. Plotnik, Y. Lumer, S. Nolte, K. G. Makris, M. Segev, M. C. Rechtsman, and A. Szameit, *Nat. Mater.* **16**, 433 (2017).
- [49] J. M. Zeuner, M. C. Rechtsman, Y. Plotnik, Y. Lumer, S. Nolte, M. S. Rudner, M. Segev, and A. Szameit, *Phys. Rev. Lett.* **115**, 040402 (2015).
- [50] K. Wang, X. Qiu, L. Xiao, X. Zhan, Z. Bian, W. Yi, and P. Xue, *Phys. Rev. Lett.* **122**, 020501 (2019).
- [51] K. Wang, X. Qiu, L. Xiao, X. Zhan, Z. Bian, B. C. Sanders, W. Yi, and P. Xue, *Nat. Commun.* **10**, 2293 (2019).
- [52] X.-Y. Xu, Q.-Q. Wang, M. Heyl, J. C. Budich, W.-W. Pan, Z. Chen, M. Jan, K. Sun, J.-S. Xu, Y.-J. Han, C.-F. Li, G.-C. Guo, arXiv:1808.03930.
- [53] W. Zhu, X. Fang, D. Li, Y. Sun, Y. Li, Y. Jing, and H. Chen, *Phys. Rev. Lett.* **121**, 124501 (2018).
- [54] X.-Y. Guo, C. Yang, Y. Zeng, Y. Peng, H.-K. Li, H. Deng, Y.-R. Jin, S. Chen, D. Zheng, and H. Fan, *Phys. Rev. Appl.* **11**, 044080 (2019).
- [55] A. M. Childs, D. Gosset, and Z. Webb, *Science* **339**, 791 (2013).
- [56] A. M. Childs, *Phys. Rev. Lett.* **102**, 180501 (2019).
- [57] Y. Wang, Y. Shang, and P. Xue, *Quantum Inf. Process* **16**, 221 (2017).
- [58] S. Dadrás, A. Gresch, C. Groiseau, S. Wimberger, and G. S. Summy, *Phys. Rev. Lett.* **121**, 070402 (2018).
- [59] E. J. Meier, F. A. An, and B. Gadway, *Phys. Rev. A* **93**, 051602(R) (2016).
- [60] F. A. An, E. J. Meier, J. Ang'ong'a, and B. Gadway, *Phys. Rev. Lett.* **120**, 040407 (2018).
- [61] E. J. Meier, F. A. An, and B. Gadway, *Nat. Commun.* **7**, 13986 (2016).
- [62] E. J. Meier, F. A. An, A. Dauphin, M. Maffei, P. Massignan, T. L. Hughes, and B. Gadway, *Science* **362**, 6417 (2018).
- [63] D. Xie, W. Gou, T. Xiao, B. Gadway and B. Yan, *npj Quantum Information* **5**, 1 (2019).
- [64] J. K. Asbóth and H. Obuse, *Phys. Rev. B* **88**, 121406(R) (2013).
- [65] J. C. Budich, Y. Hu and P. Zoller, *Phys. Rev. Lett.* **118**, 105302 (2017).
- [66] S. Mukherjee, H. K. Chandrasekharan, P. Öhberg, N. Goldman, and R. R. Thomson, *Nat. Commun.* **9**, 4209 (2018).
- [67] See Supplemental Materials for details.

## Supplemental Materials for “Topological quantum walks in momentum space with a Bose-Einstein condensate”

In this Supplemental Materials, we provide details for the derivation of the effective Hamiltonian and the topological invariants. We also provide additional simulation and experimental data demonstrating time-averaged mean chiral displacement, the detection of topological edge states, and the comparison between the full and effective Hamiltonians.

### DERIVATION OF THE EFFECTIVE HAMILTONIAN

In this section, we derive, from the full Hamiltonian, the effective Hamiltonian as shown in Eq. (1) of the main text. Following the experimental setup illustrated in Fig. 1 of the main text, we start from the single-particle Hamiltonian under the dipole approximation

$$\hat{H} = \frac{\hat{\mathbf{p}}^2}{2M} + \hbar\omega_e |e\rangle \langle e| + \hbar\omega_g |g\rangle \langle g| + \mathbf{d} \cdot \mathbf{E}, \quad (\text{S1})$$

where  $|g\rangle$  ( $|e\rangle$ ) is the atomic ground (excited) state with energy  $\hbar\omega_g$  ( $\hbar\omega_e$ ),  $M$  is the atomic mass, and  $\mathbf{d}$  is the electric dipole moment. The electric field is given by  $\mathbf{E} = \mathbf{E}_+ + \mathbf{E}_-$ , with

$$\mathbf{E}_+ = \mathbf{E}_+ \cos(\mathbf{k}_+ \cdot \mathbf{x} - \omega_+ t + \phi_+), \quad (\text{S2})$$

$$\mathbf{E}_- = \sum_i \mathbf{E}_i \cos(\mathbf{k}_i \cdot \mathbf{x} - \omega_i t + \phi_i), \quad (\text{S3})$$

where  $\Omega_+ = \langle e | \mathbf{d} \cdot \mathbf{E}_+ | g \rangle / \hbar$ ,  $\Omega_i = \langle e | \mathbf{d} \cdot \mathbf{E}_i | g \rangle / \hbar$ , and  $\omega_+$  and  $\omega_i$  ( $\phi_+$  and  $\phi_i$ ) are the frequencies (phases) of acoustic-optical modulated Raman lasers. According to our experimental configuration (see Fig. 1 of the main text), we write  $\mathbf{k}_+ = k\mathbf{e}_x$ ,  $\mathbf{k}_i \simeq -k\mathbf{e}_x$ , and  $\Delta \equiv \omega_{eg} - \omega_+ \simeq \omega_{eg} - \omega_i$  with  $\omega_{eg} \equiv \omega_e - \omega_g$ . Here  $\mathbf{e}_x$  is the unit vector along the  $x$  direction.

Without loss of generality, we assume that the Rabi frequencies  $\Omega_+$  and  $\Omega_i$  are real, so the Hamiltonian can be written as

$$\begin{aligned} \hat{H} = & \frac{\hat{\mathbf{p}}^2}{2M} + \hbar\omega_e |e\rangle \langle e| + \hbar\omega_g |g\rangle \langle g| \\ & + \hbar \left[ \Omega_+ \cos(kx - \omega_+ t + \phi_+) + \sum_i \Omega_i \cos(-kx - \omega_i t + \phi_i) \right] \\ & \times (|e\rangle \langle g| + |g\rangle \langle e|). \end{aligned} \quad (\text{S4})$$

We then apply the rotating-wave approximation, adiabatically eliminate the excited state  $|e\rangle$ , and expand the external motion of the ground state in the discretized momentum lattice with  $|\psi\rangle = \sum_n c_n e^{i2nkx} |n\rangle \otimes |g\rangle$  ( $n \in$

$\mathbb{Z}$ ). The resulting effective ground-state Hamiltonian becomes

$$\begin{aligned} \hat{H}_{\text{eff}} = & \sum_n 4n^2 E_r |n\rangle \langle n| \\ & + \frac{\hbar}{4\Delta} \sum_n \Omega_+ \Omega_n e^{-i(\omega_+ - \omega_n)t} e^{i(\phi_+ - \phi_n)} |n+1\rangle \langle n| \\ & + \frac{\hbar}{4\Delta} \sum_n \Omega_+ \Omega_n e^{i(\omega_+ - \omega_n)t} e^{-i(\phi_+ - \phi_n)} |n\rangle \langle n+1|. \end{aligned} \quad (\text{S5})$$

Experimentally, we tune the effective Rabi frequencies of all Raman processes to be of the same magnitude, such that  $\Omega = \frac{\Omega_n \Omega_+}{2\Delta}$ . We then have

$$\begin{aligned} \hat{H}_{\text{eff}}^I = & \sum_n \left( \frac{\hbar\Omega}{2} e^{i(2n+1)\frac{4E_r}{\hbar}t} e^{-i(\omega_+ - \omega_i)t} e^{i\varphi_n} |n+1\rangle \langle n| \right. \\ & \left. + \frac{\hbar\Omega}{2} e^{-i(2n+1)\frac{4E_r}{\hbar}t} e^{i(\omega_+ - \omega_i)t} e^{-i\varphi_n} |n\rangle \langle n+1| \right), \end{aligned} \quad (\text{S6})$$

where  $\varphi_n = (\phi_+ - \phi_n)$ , and we have taken the appropriate interaction picture.

The effective Hamiltonian (S6) can be further simplified by neglecting non-resonant terms. Experimentally, we choose  $\Omega \ll 4E_r$ , such that only resonant terms have significant contribution in the dynamics. The resulting Hamiltonian becomes

$$\hat{H}_{\text{eff}}^I = \sum_n \left( \frac{\hbar\Omega}{2} e^{i\varphi_n} |n+1\rangle \langle n| + H.c. \right), \quad (\text{S7})$$

which is a tight-binding Hamiltonian on a momentum lattice. In the experiment, we set  $\varphi_n = 0$  for all  $n$ .

We now consider the periodic switching of the Raman couplings, due to the step functions imposed by the radio-frequency (RF) driver. Denoting the pulse durations when the even- (odd-) frequency components are switched on as  $t_w$  ( $t_q$ ), we map the effective Hamiltonian to a Su-Schrieffer-Heeger (SSH) model in momentum space with periodically driven coefficients

$$\hat{H} = w(t) \sum_m |m, b\rangle \langle m, a| + q(t) \sum_m |m+1, a\rangle \langle m, b| + H.c., \quad (\text{S8})$$

where the mapping between  $|m, a(b)\rangle$  as well as the coefficients  $w(t)$  and  $q(t)$  are given in the main text.

### TOPOLOGICAL INVARIANTS OF DISCRETE-TIME QUANTUM WALKS

The discrete-time quantum walk governed by  $U = Q(\theta_2)W(\theta_1)$  supports Floquet topological phases, whose

topological invariants can be calculated by going to different time frames. These time frames are respectively governed by the Floquet operators

$$U_1 = W\left(\frac{\theta_1}{2}\right)Q(\theta_2)W\left(\frac{\theta_1}{2}\right), \quad (\text{S9})$$

$$U_2 = Q\left(\frac{\theta_2}{2}\right)W(\theta_1)Q\left(\frac{\theta_2}{2}\right). \quad (\text{S10})$$

The topology of these Floquet operators are characterized by their associated winding numbers ( $C_1, C_2$ ). To calculate the winding numbers, we perform Fourier transforms on  $U_1$  and  $U_2$ , and write their Fourier components as

$$U_1 = d_0^{(1)}\sigma_0 - id_1^{(1)}\sigma_x - id_2^{(1)}\sigma_y - id_3^{(1)}\sigma_z, \quad (\text{S11})$$

$$U_2 = d_0^{(2)}\sigma_0 - id_1^{(2)}\sigma_x - id_2^{(2)}\sigma_y - id_3^{(2)}\sigma_z, \quad (\text{S12})$$

where  $\sigma_{x,y,z}$  are Pauli matrices,  $I$  is a two-by-two identity matrix, and the coefficients  $d_i^{(1,2)}$  ( $i = 0, 1, 2, 3$ ) are

$$\begin{aligned} d_0^{(1)} &= -\cos \tilde{k} \sin \theta_1 \sin \theta_2 + \cos \theta_1 \cos \theta_2, \\ d_1^{(1)} &= -\cos \theta_2 \sin \theta_1 - \cos \tilde{k} \cos \theta_1 \sin \theta_2, \\ d_2^{(1)} &= -\sin \tilde{k} \sin \theta_2, \\ d_3^{(1)} &= 0, \end{aligned} \quad (\text{S13})$$

and

$$\begin{aligned} d_0^{(2)} &= -\cos \tilde{k} \sin \theta_1 \sin \theta_2 + \cos \theta_1 \cos \theta_2, \\ d_1^{(2)} &= \cos^2 \tilde{k} \sin \theta_1 (1 - \cos \theta_2) - \sin \theta_1 - \cos \tilde{k} \cos \theta_1 \sin \theta_2, \\ d_2^{(2)} &= -\sin \tilde{k} (\cos \theta_1 \sin \theta_2 - \cos \tilde{k} \sin \theta_1 + \cos \tilde{k} \cos \theta_2 \sin \theta_1) \\ d_3^{(2)} &= 0. \end{aligned} \quad (\text{S14})$$

Here  $\tilde{k}$  belongs to the first Brillouin zone of the momentum lattice.

The winding numbers are calculated as

$$C_\alpha = \frac{1}{2\pi} \int d\tilde{k} \frac{-d_2^{(\alpha)} \frac{\partial d_1^{(\alpha)}}{\partial \tilde{k}} + d_1^{(\alpha)} \frac{\partial d_2^{(\alpha)}}{\partial \tilde{k}}}{d_2^{(\alpha)2} + d_1^{(\alpha)2}} \quad (\alpha = 1, 2). \quad (\text{S15})$$

Alternatively, we define the topological invariants

$$\begin{aligned} C_0 &= \frac{C_1 + C_2}{2}, \\ C_\pi &= \frac{C_1 - C_2}{2}, \end{aligned} \quad (\text{S16})$$

which directly correspond to topological edge states with quasienergies  $\epsilon = 0$  and  $\epsilon = \pi$ , respectively, through the bulk-boundary correspondence. The topological phase diagram for  $(C_0, C_\pi)$  are shown in Fig. 3 of the main text.

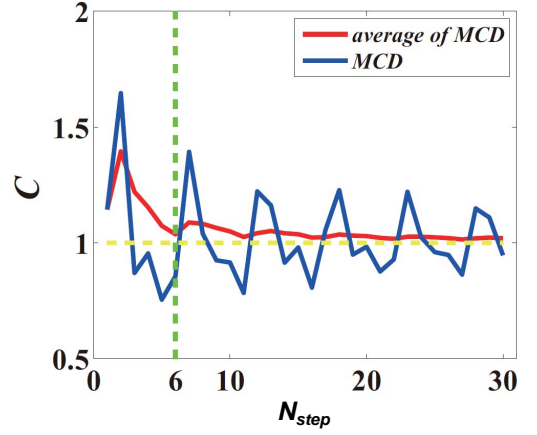


FIG. S1. Comparison of MCD and A-MCD. The blue line shows MCD versus discrete time step  $t/T$ . The red line shows A-MCD, which converges faster than the MCD. The yellow dashed line shows the ideal winding number  $C_1$ . The parameters are  $(\theta_1, \theta_2) = (3\pi/32, 9\pi/32)$ . The green dashed line indicates the experimentally implemented time step  $N_{\text{step}} = 6$ .

### TIME AVERAGED MEAN CHIRAL DISPLACEMENT

Topological invariants can be directly probed in quantum-walk dynamics through mean chiral displacement (MCD), defined as

$$C_{1,2}(t) = 2 \sum_m m [P_{m,a}^{(1,2)}(N_{\text{step}}) - P_{m,b}^{(1,2)}(N_{\text{step}})], \quad (\text{S17})$$

where  $P_{m,a(b)}^\alpha(N_{\text{step}})$  is the atom population in  $|m, a(b)\rangle$  at the  $N_{\text{step}}$ -th step under  $U_\alpha$ . In our experiment, we measure the time-averaged mean chiral displacement (A-MCD) instead, which converges faster to the corresponding winding number. The A-MCD is defined as

$$\bar{C}_{1,2}(t) = \frac{2}{N} \sum_{N_{\text{step}}, m} m [P_{m,a}^{(1,2)}(N_{\text{step}}) - P_{m,b}^{(1,2)}(N_{\text{step}})], \quad (\text{S18})$$

where  $N_{\text{step}} = 1, 2, \dots, N$ .

In Fig. S1, we show a numerical calculation comparing MCD and A-MCD for a finite-step quantum walk governed by the effective Hamiltonian Eq. (S8). Whereas oscillations in the MCD persist into longer times, A-MCD already converges at the sixth step. Apparently, the fast convergence of A-MCD stems from the oscillatory behavior of MCD at intermediate times. Further, from an experimental point of view, A-MCD helps to average out the inevitable fluctuations in the durations of Raman pulses. As such, it is preferable to probe A-MCD for the direct measurement of winding numbers.

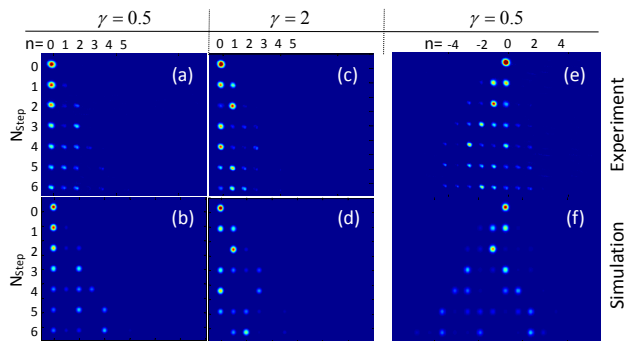


FIG. S2. (Color online) Experimental detection of topological edge states. (a)(b) Dynamics under  $U_1$  with an open boundary at  $n = 0$ . The bulk is topologically non-trivial with  $\gamma = 0.5$  ( $\gamma = \theta_1/\theta_2$ ) and  $C_1 = 1$ . (c)(d) Dynamics under  $U_1$  with an open boundary at  $n = 0$ . The bulk is topologically trivial with  $\gamma = 2$  and  $C_1 = 0$ . Localization of atom population near  $n = 0$  is observed in (a)(b), but not in (c)(d), particularly for the last step. (e)(f) Dynamics under  $U_1$  with no boundaries near  $n = 0$ . The bulk is topologically non-trivial with  $\gamma = 0.5$  and  $C_1 = 1$ . Compared to (a)(b), atoms are not localized near  $n = 0$ .

### DETECTING OF EDGE STATES

A prominent property of topological phases, robust edge states exist at boundaries between bulks with different topological invariants. The presence of edge states give rise to local population accumulation in quantum-walk dynamics, which have been used as a signature for topological quantum walks. For our system, we create an open boundary near  $n = 0$  by turning off RF components in the AOM driver corresponding to sites with  $n < 0$ . In Fig. S2, we show measured atom population along the momentum lattice at different times of the dynamics. Under an open boundary condition, local atom population should accumulate near  $n = 0$  when the bulk has finite winding numbers. In contrast, when the bulk winding numbers vanish, atom population should become extended in momentum space at long times. As illustrated in Fig. S2(a)(c), difference in the local-population accumulation near the boundary for topological trivial and non-trivial bulks is becoming discernable at the sixth step, albeit larger steps are needed to fully differentiate the two cases. For comparison, we plot in Fig. S2(e)(f) dynamics of a homogeneous quantum walk. Despite finite winding numbers in the bulk, atom population becomes extended at long times, due to the absence of any boundaries.

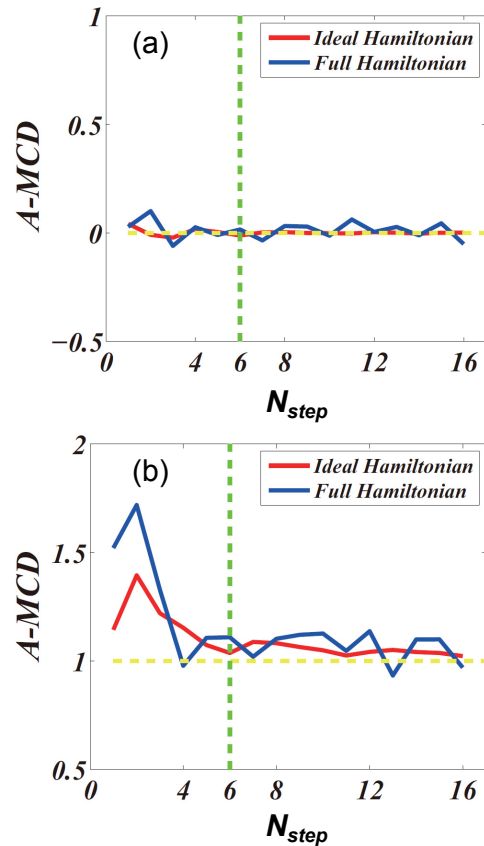


FIG. S3. A-MCD for (a)  $(\theta_1, \theta_2) = (5\pi/16, \pi/16)$ , and (b)  $(\theta_1, \theta_2) = (3\pi/32, 9\pi/32)$ . The red line shows A-MCD under the simplified Hamiltonian Eq. (S8). The blue line shows A-MCD of the full Hamiltonian Eq. (S6). The green dashed line indicates the experimentally implemented time step  $N_{\text{step}} = 6$ .

### COMPARISON OF THE FULL HAMILTONIAN AND THE SIMPLIFIED HAMILTONIAN

In this section, we compare dynamics under the full Hamiltonian in Eq. (S6) and that under the simplified periodically driven SSH model Eq. (S8). Using numerical simulations, we demonstrate that, under our typical experimental conditions, it is reasonable to neglect the non-resonant terms in Eq. (S6), a crucial approximation leading to the implementation of discrete-time quantum-walk dynamics in momentum space.

We adopt the time frame governed by  $U_1$ , and choose two sets of parameters:  $(\theta_1, \theta_2) = (5\pi/16, \pi/16)$  with  $C_1 = 0$ , and  $(\theta_1, \theta_2) = (3\pi/32, 9\pi/32)$  with  $C_1 = 1$ . In Fig. S3, we plot the resulting A-MCD under the ideal Hamiltonian in red, and the A-MCD under the full Hamiltonian in blue. In both cases, the two results lie close to one another and to the respective winding number  $C_1$  (yellow dashed line) up to sixteen time steps.